PAPER

Check for updates

Revealing the anisotropic phonon behaviours of layered SnS by angle/temperature-dependent Raman spectroscopy†

Xiangnan Gong, ✶*a Ting Yan,b Jue Li,b Jie Liu,a Hanjun Zou,a Bin Zhang,a Hong Wu,*c Zizhen Zhou*b and Xiaoyuan Zhou ab

Tin sulfide (SnS), a IV–VI group layered compound, has attracted much attention because of its excellent thermoelectric properties along the crystallographic *b*-axis. However, there are few reports on the identification of its in-plane orientation. We observe a strong anisotropy of the in-plane Raman signal in bulk SnS. With the help of *ab initio* calculations, the vibrational symmetry of each observed Raman mode in the cleaved (00*l*)-plane is consistent with the experimental values. The angle-resolved polarized Raman spectroscopy, combined with electron backscattered diffraction technology, is utilized to systematically investigate the in-plane anisotropy of the phonon response and then determine the in-plane orientation. Furthermore, the temperature-dependent and laser-power-dependent Raman scattering analyses reveal that the adjacent layers in the SnS crystals show a relatively weak van der Waals interaction. These findings could provide much-needed experimental information for future applications related to the anisotropic transport properties of SnS single crystals.

Introduction

Orthorhombic tin sulfide (SnS), a binary IV–VI group chalcogenide material consisting of earth-abundant, low-cost and nontoxic elements, has attracted growing attention owing to its various potential applications.[1–4] In particular, many works have focused on its thermoelectric applications due to the theoretically predicted excellent thermoelectric performance. SnS exhibits a layered structure with strong Sn–S bonds forming puckered *a–b* sheets, which stack along the *c*-axis with weak intermolecular interactions.[5] Because of this special crystal structure, its properties usually show strong anisotropy along each axis.[1,6] Hence, it is of vital importance to determine the orientation of SnS single crystal, which has a great influence on the properties and the applications in devices. Generally, the X-ray crystal orientation apparatus is used to determine crystal orientation of large-size bulk materials, but cannot deal with the 2D layered materials with in-plane anisotropy.[1] The angle-resolved polarized Raman spectroscopy (ARPRS) is anticipated to solve this problem because it is simple, nondestructive, fast

and accurate.[7,8] Currently, many works have verified the practicability of this method by integrating with angular resolved polarization conductance techniques,[8–10] electron microscopy,[11,12] optical microscopy,[11,12] X-ray diffraction (XRD),[13] and quantitative atomic-resolution force image.[14] However, to the best of our knowledge, there are few reports focusing on the application of ARPRS along with electron backscattered diffraction (EBSD) technology, which can be used to identify the in-plane direction of the layered single crystals such as SnS in a more macroscopic and simple operation.

In this study, high-quality bulk SnS single crystals were successfully synthesized using a modified Bridgman method, the crystal structure was characterized by single crystal X-ray diffractometer (SCXRD) and high-resolution transmission electron microscopy (HRTEM). Besides, a systematic Raman study was implemented on SnS single crystal from both theoretical and experimental perspectives. The observed Raman modes of B_{3g}^1 (49 cm^{-1}), A_g^1 (95 cm^{-1}), B_{3g}^2 (164 cm^{-1}), A_g^2 (192 cm^{-1}), and A_g^3 (218 cm^{-1}) agree with the calculated results by density functional theory (DFT) method. Moreover, the optical anisotropy property of SnS single crystal was systemically investigated by ARPRS technology, in which Raman intensity shows a strong sensitivity to crystal orientation, and its anisotropy is associated with the polarization configurations and photon energies. Combined with EBSD technology, the ARPRS was successfully employed to confirm the in-plane orientation of the SnS single crystal, which would be efficiently to identify the crystal orientation. Finally, temperature-dependent Raman spectroscopy can be used to study the

aAnalytical and Testing Center, Chongqing University, Chongqing 401331, China. E-mail: carefen82082022@163.com

bCollege of Physics, Chongqing University, Chongqing 401331, China. E-mail: zzzhou@cqu.edu.cn

cSchool of Science, Chongqing University of Posts and Telecommunications, Chongqing 400065, China. E-mail: wuhong@cqupt.edu.cn

thermal expansion of SnS crystals with anisotropic characteristics. We believe that our findings will provide new insights into the experimental information of layered materials.

Experimental

SnS single crystals were synthesized using the method as previously reported.[6] The starting materials of high-purity of Sn granules (99.999%), S powder (99.99%) were weighed intensively according to the stoichiometry of Sn : S = 1 : 1 under argon atmosphere. Mixtures were sealed in cone-shaped quartz tubes under a pressure ($\sim5 \times 10^{-4}$ Pa) and encased in another larger quartz tube, evacuated again and flame-sealed. The tubes were heated up to 1273 K over 12 h, and soaked at that temperature for 15 h. SnS single crystals were grown when the furnace cooled to 1100 K at a rate of 1.5 mm h^{-1} subsequently. Excellent quality of SnS single crystals with diameter of 15 mm and height of 45 mm were grown, as shown in Fig. S1a (ESI†).

The crystal structure was determined by an Rigaku Super-Nova diffractometer (Mo Kα radiation, $\lambda = 0.71073$ Å) at room temperature (295 K). The X-ray data collection, intensity data

reduction and empirical absorption correction were conducted using CrysAlis^{Pro} software. Crystal structures were refined with SHELXL,[15] operated using the Olex2 program.[16] All atoms were refined anisotropically. The resulting cell parameters, selected atomic coordinates, bond lengths, and bond angles are listed in Tables 1 and S1, S2.† The high angle annular dark field (HAADF), selected area electron diffraction (SAED) and X-ray energy dispersive spectroscopy (EDS) mapping experiments were performed on Thermo Scientific Talos F200S G2 at 200 kV to investigate the microstructure of the samples.

EBSD was collected with a NordlysMax2 detector (Oxford Instruments) integrated with a JEOL JSM-7800F FESEM system. The acceleration voltage was 15 kV and the sample tilted at 70°. The crystallographic orientation data was collected using the Aztec EBSD data acquisition software and post-analyzed using the HKL Channel 5 package for crystallographic orientation.

Raman spectra were performed using a HORIBA JobinYvon HR Evolution confocal Raman spectroscopy system with the excitation wavelength of 532 nm and 632.8 nm. High-resolution spectra were collected using a 100× long work distance (NA = 0.9) objective and recorded with 1800 groove mm^{-1} holographic grating. Based on
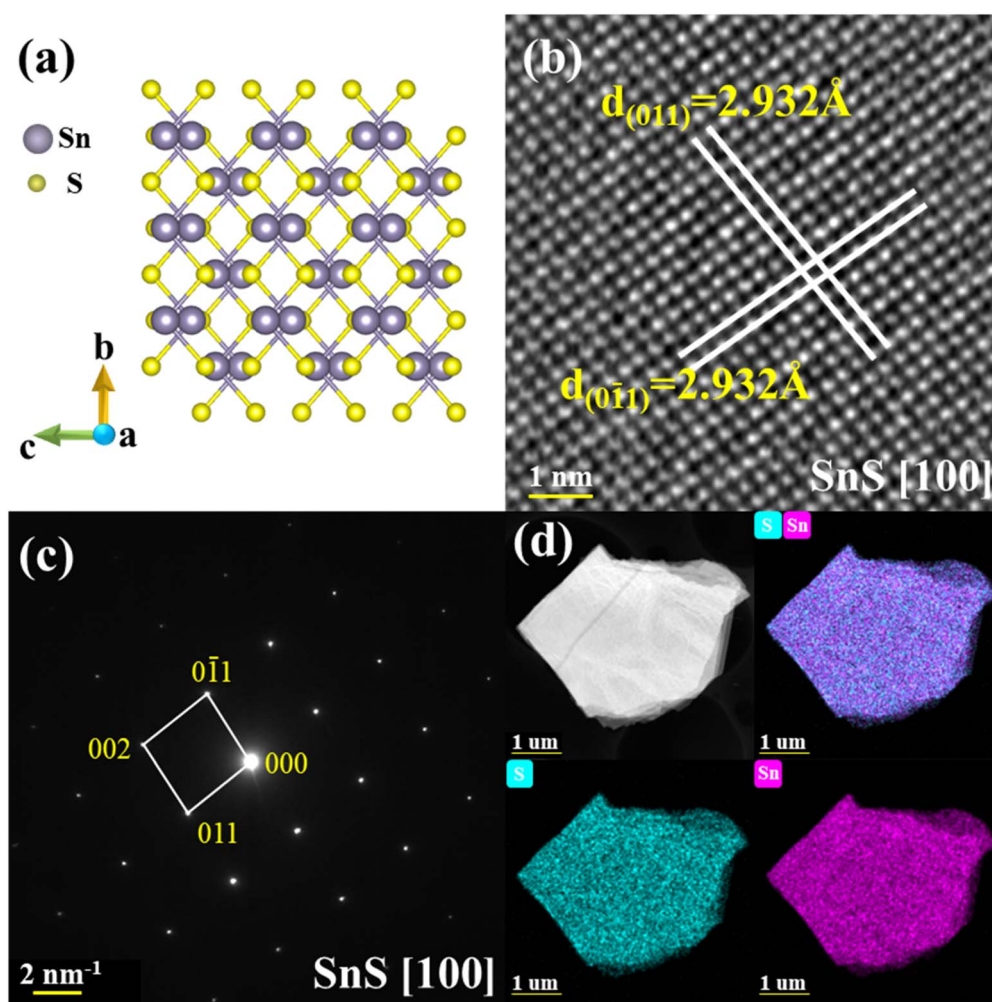

Fig. 1 .Structural characterization of SnS single crystal along the [100] direction. (a) The atomic arrangement of SnS (*Pnma*). (b) The HAADF image. (c) The SAED pattern. (d) STEM–EDS mapping.

the backscattering geometry of ARPRS measurements, the polarization direction of the incident laser was fixed to be vertical (along *y*-axis) by using a polarizer in the beam path; while the parallel and cross configurations were set by the directions of the analyzer along *y*-axis or *x*-axis before the spectrometer entrance, corresponding to vertical or horizontal, respectively. The samples were placed on a rotation stage and clockwise rotated around the *z*-axis by an angle *θ* between the laser polarization direction and *a*-axis (zigzag direction) of the crystal coordinates. The schematic diagram of the set-up is shown in Fig. S5 (ESI†). For temperature-dependent Raman measurements, a Janis ST-500 stage was conducted in the temperature range from 77 K to 400 K under 2×10^{-5} mba. In all cases, a very low incident light power below 0.5 mW was used to avoid any photodegradation of the samples, meanwhile 300 s exposure-time was used to obtain good signal-to-noise ratio spectrums. For laser-power-dependent Raman experiments, the laser power is set by the laser power supply and a set of neutral-density filters together, then the laser power is detected under the objective by the Newport 843-R power-meter with 818-UV head. All spectra had been calibrated by mercury peak at 546.07 nm for 532 nm laser excitation, and neon peaks at 640.22 nm and 638.29 nm for 632.8 nm laser excitation, respectively.

First principles calculation based on density functional theory (DFT) and augmented plane wave (PAW) method was performed in the Vienna *Ab initio* Simulation Package (VASP).[17–19] The exchange-correlation functional was defined by a generalized gradient approximation (GGA) of Perdew–Burke–Ernzerhof (PBE).[20] The convergence of the total energies was set to be 1×10^{-8} eV. The geometry was fully relaxed until the forces on the atoms were less than 1×10^{-4} eV Å^{-1} with an energy cutoff 500 eV. For the Brillouin zone integrations, the Monkhorst–Pack (MP) *K*-points scheme of $3 \times 9 \times 9$ was adopted. The phonon spectrum of SnS was calculated using the frozen phonon method using a $2 \times 2 \times 2$ supercell, which is implemented in the Phonopy package.[21]

Results and discussion

Tin sulfide crystallizes in an orthorhombic space group *Pnma* (No. 62) along the [100] direction, with the lattice parameters of $a = 11.1935(15)$ Å, $b = 3.9833(4)$ Å, $c = 4.3293(5)$ Å, and $\alpha = \beta = \gamma = 90°$, which is verified by SCXRD as shown in Fig. 1a. Details of the diffraction data and crystal structure refinement are summarized in Table 1. Each Sn atom is coordinated by six S atoms in a highly distorted octahedral geometry. Owing to this strong distortions, Sn atom is displaced toward one of the faces of the octahedra, it leads to three short Sn–S bonds of ~2.626 Å and three long Sn–S bonds of ~2.664 Å, being responsible for the strong lattice anharmonicity.[22] There are two SnS layers in a unit cell and one of the long Sn–S bond resides on the neighboring layer interacted by the weak van der Waals forces, as displayed in Fig. S1a and Table S1 (ESI†). Fig. 1b and c display the HAADF image and corresponding SAED pattern indexed to the zone of [100], respectively. Based on the HAADF image, the *d*-spacing of interplanar planes was measured as ~2.932 Å of both (011) and (01$\bar{1}$). Additionally, the clear Bragg spots of [100] SAED pattern without the appearance of any extra spots indicate

the single crystal of as-synthesized SnS samples. The elements were evenly distributed and further confirmed by the direct evidence of STEM-EDS mappings, as depicted in Fig. 1d. Furthermore, XRD experiment was carried out to identify the crystal structure of as-grown samples. As shown in Fig. S2a (ESI†), two main XRD peaks belong to the (400) and (800) planes obtained on the (100) cleavage surface. Additionally, we collected powder XRD patterns of as-grown samples in Fig. S2b (ESI†) for phase identification. All major diffraction peaks can be indexed to the orthorhombic structure (PDF#01-073-1859) with the space group of *Pnma*, indicating no secondary phases.

A unit cell of SnS contains 8 atoms, which leads to theoretically 24 vibrational modes in the phonon dispersions. The crystal symmetry determined irreducible representation of D_{2h} at the center of the Brillouin zone (*Γ* point) is represented as:[23,24]

$$\Gamma = 4A_g + 2B_{1g} + 4B_{2g} + 2B_{3g} + 2A_u + 4B_{1u} + 2B_{2u} + 4B_{3u}$$

Also, the phonon dispersions calculated by the DFT method are shown in the left side of Fig. 2a, in which the 24 simulated curves are displayed as consistent with those previously reported.[25] Three colored curves at the bottom represent the acoustic phonon vibrations including two transverse acoustic phonons (TA and TA′) and one longitudinal acoustic phonon (LA), while the other 21

Table 1 Crystal data and structure refinement for SnS at room temperature

Empirical formula	SnS
Formula weight	150.75
Temperature	295(2) K
Radiation	Mo Kα
Wavelength	0.71073 Å
Crystal system	Orthorhombic
Space group	*Pnma*
Unit cell dimensions	$a = 11.1935(15)$ Å
	$b = 3.9833(4)$ Å
	$c = 4.3293(5)$ Å
	$\alpha = \beta = \gamma = 90°$
Cell volume	193.03(4) Å^{-3}
Z	4
Calculated density	5.187 g cm^{-3}
Absorption coeefficient	13.764 mm^{-1}
F(000)	264.0
Crystal size	$0.15 \times 0.12 \times 0.09$ mm^3
Two-theta range for data collection	$7.28° \leq 2\theta \leq 52.74°$
Index ranges	$-13 \leq h \leq 10$
	$-4 \leq k \leq 3$
	$-5 \leq l \leq 5$
Reflections collected	604
Completeness to 100%	$\theta = 26.37°$
Absorption correction	Multi-scan
Max. and min. transmission	1.000 and 0.300
Refinement method	Full-matrix least-squares on F^2
Independent reflections	224 [$R_{int} = 0.0273$, $R_{sigma} = 0.0334$]
Data/restraints/parameters	224/0/13
Goodness-of-fit on F^2	1.196
Final *R* indexes [$I \geq 2\sigma(I)$]	$R_1 = 0.0448$, w$R_2 = 0.1079$
Final *R* indexes [all data]	$R_1 = 0.0498$, w$R_2 = 0.1135$
Largest diff. peak and hole	2.59 and −1.68 e Å^{-3}

vibration modes belong to the optical branch. Among them, 5 Raman active modes, B_{3g}^1, A_g^1, B_{3g}^2, A_g^2, and A_g^3 are specially marked as red squares at gamma (Γ) point and corresponding Raman modes have been carried out based on our back-scattering geometry configuration and the cleavage (100) plane, located at 49, 95, 164, 192 and 218 cm^{-1} at room temperature, respectively. The corresponding molecular vibration is exhibited in Fig. 2b. In addition, the phonon density of states (DOS) of SnS crystal was displayed on the right side of Fig. 2a, which clearly shows that the phonon DOS below 150 cm^{-1} mainly contributed by the heavier Sn atom (green line), whereas the DOS above 150 cm^{-1} primarily results from the S element with lighter atomic mass (red line). As previously reported, many materials with low-symmetric structures exhibit anisotropic transport properties, including the phonon vibrational properties.[24,26–28] Raman spectroscopy could provide fruitful information about crystal structures and phonon properties. We carried out ARPRS experiments on SnS single crystals to study its phonon vibrational anisotropy based on the backscattering geometry. The incident laser polarization (e_i) was kept along the horizontal direction (x-direction as denoted in Fig. S1a†), while the scattered Raman signals polarization (e_s) was parallel or perpendicular to the incident laser polarization by using a linear analyzer before the spectrometer entrance slit. Fig. 3a depicts the Raman spectra of SnS measured at an angle 0° under three kinds of polarized configurations including unpolarized, parallel and perpendicular. Five Raman peaks can be detected in unpolarized

configuration and assigned as A_g and B_{3g} modes, but the intensity of some Raman peaks varies in parallel and perpendicular configurations, showing the polarization property. Fig. 3b and c present the false-color plots of parallel and perpendicular polarized Raman intensities with the rotation angle ranging from 0° to 360°, respectively. It is observed that B_{3g} modes exhibit a 4-folded shape (*e.g.*, 49 and 164 cm^{-1}) and A_g modes yield a 2-folded shape (*e.g.*, 95 and 192 cm^{-1}) under both parallel and perpendicular polarization configurations. Compared to the two false-color maps, the relative intensity of B_{3g}^1 mode is strongest in parallel polarization configurations, while the A_g^1 mode is the strongest in perpendicular polarization configurations. These two modes can be used to analysis the angle orientation. It should be noted that B_{3g}^1 mode is almost disappearing in perpendicular polarization configurations and can still hold the 4-folded shape. The ARPRS experiment of SnS crystal was also excited under 632.8 nm laser, as shown in Fig. S3 (ESI†). These results clearly reveal that the polarized Raman spectra are strongly dependent on crystalline orientation. To provide preliminary insight into the phenomenon, the intensity I of Raman peaks can be expressed as:[29]

$$I \propto |e_i \times R \times e_s^{\mathrm{T}}|^2$$

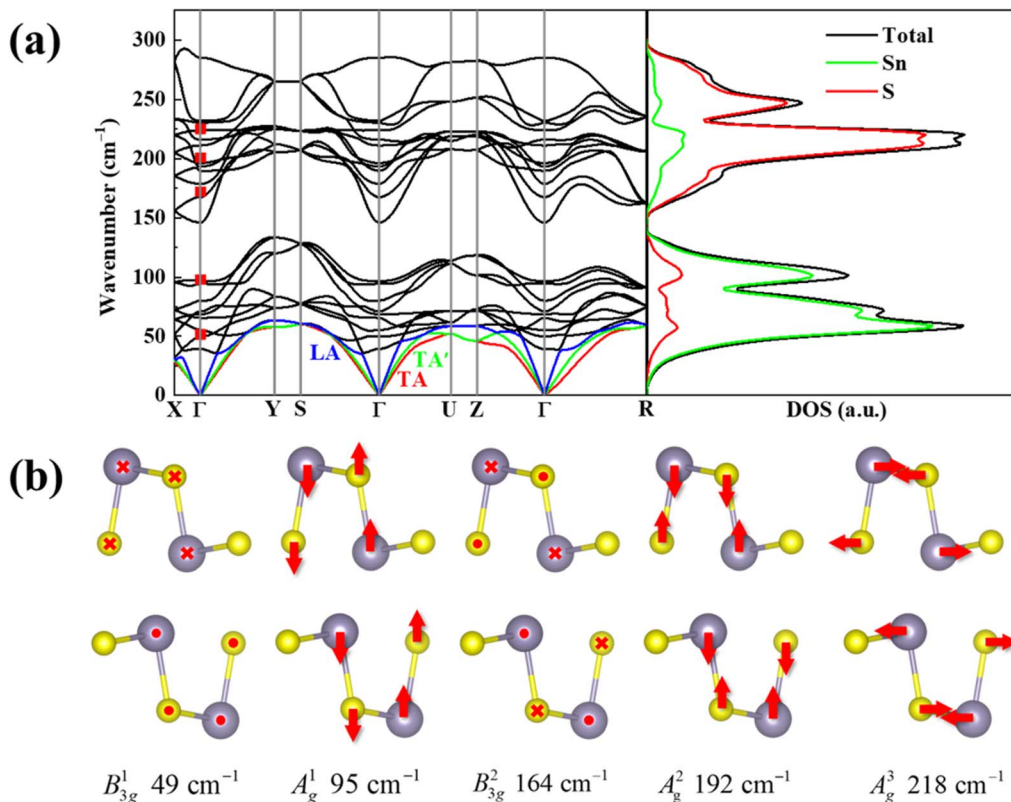The Raman tensor R can be found in the table of point group D_{2h}:

Fig. 2 .(a) Phonon dispersion curves of SnS calculated by DFT method for the cleavage plane. Five detected Raman modes are marked as red squares at Γ point. (b) Side views of the atomic vibrations of the 5 Raman active modes measured in the range of 40–300 cm^{-1}. Two adjacent layers of SnS are represented as two rows in the figures.
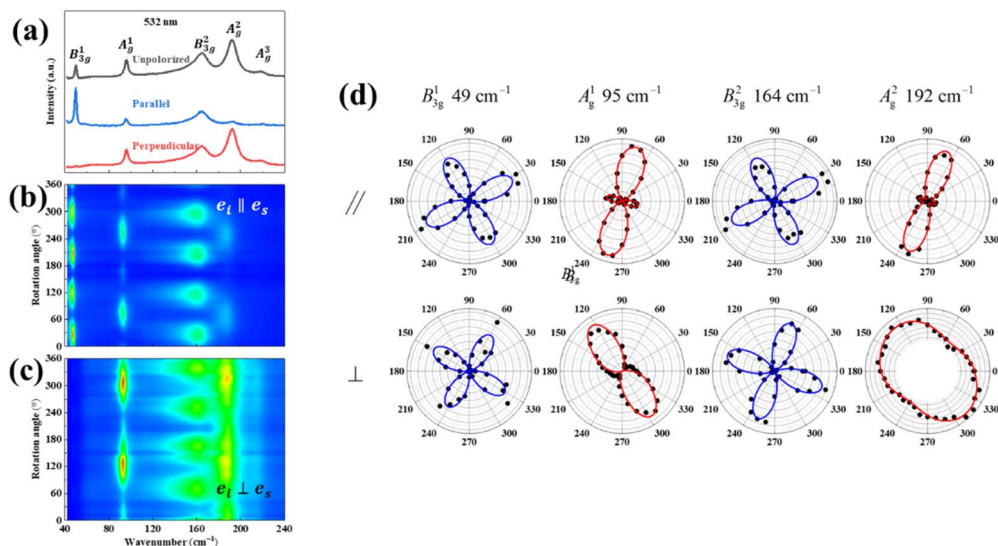
Fig. 3 .ARPRS of SnS single crystal on the cleavage plane excited by 532 nm. (a) Measuring Raman spectra at a 0° angle under unpolarized, parallel and perpendicular configurations. False-colour plots of polarized Raman intensities under (b) parallel and (c) perpendicular polarization configurations, respectively. (d) The corresponding ARPRS intensities in parallel and perpendicular polarization configurations (the red and blue lines represent B_{3g} and A_g modes, respectively).

$$R(A_g) = \begin{pmatrix} A & 0 & 0 \\ 0 & B & 0 \\ 0 & 0 & C \end{pmatrix} \text{ and } R(B_{3g}) = \begin{pmatrix} 0 & 0 & 0 \\ 0 & 0 & D \\ 0 & D & 0 \end{pmatrix}$$

The polarization vector for incident light is $e_i = (0 \cos\theta \sin\theta)$. The $e_s = (0 \cos\theta \sin\theta)$ or $e_s = (0 -\sin\theta \cos\theta)$ under parallel or perpendicular polarization configuration for scattered light, respectively, where θ is the angle between the incident laser polarization and x-direction of the SnS crystal. The intensities for each mode can be calculated as follows:

$$I(A_g, \parallel) \propto (B \cos^2\theta + C \sin^2\theta)$$

$$I(B_{3g}, \parallel) \propto D^2 \sin^2 2\theta$$

$$I(A_g, \perp) \propto \frac{(C - B)^2}{4} \sin^2 2\theta$$

$$I(B_{3g}, \perp) \propto D^2 \cos^2 2\theta$$

where $\parallel$ and $\perp$ stand for the parallel and perpendicular polarizations, respectively. As can be seen from Fig. 3d, the B_{3g} modes (fitted by blue lines) yield 4-fold symmetry with maximum intensity angles 30°, 120°, 210° and 300° for parallel polarization configuration, and 60°, 150°, 240° and 330° for perpendicular polarization configuration. While for A_g modes (fitted by red lines), they show quasi-2-folded symmetry, with maximum intensity angles 75° and 255° for parallel polarization configuration, 135° and 315° for perpendicular polarization configuration. After the intensity fitting for B_{3g}^1, its maximum value appears at

27.4°, which is 17.6° away from the theoretical value of 45°, while for A_g^1, its maximum value appears at 124.0°, which is 11.0° away from the theoretical value of 135°. We infer that the in-plane deflection direction of the SnS crystal determined by ARPRS method is 14.3 (±3.3). Our experimental results are in well accordance with the relationship between Raman tensors and laser polarizations, and also imply the noteworthy anisotropic structure of SnS, which could further be used to conveniently and rapidly identify the in-plane orientation of other van der Waals layered materials. Similar applications have been previously observed in many other TMDs.[24] Therefore, the ARPRS technique is a quick and easy way to confirm the crystal orientation.

In order to effectively utilize ARPRS technology to identify the in-plane orientation of SnS crystal, we also confirm crystal orientation by EBSD technology, because it can be used to determine the orientation of small grains in nano films.[30–34] Fig. 4a shows the inverse pole figures (IPF) coloring of each axis, and the chromaticity coordinates are along z-axis (100-direction), suggesting a high degree of orientation and large size of the crystal with no grain boundary in sight.[32] As can be estimated from the pole figures (PF) in Fig. 4b, the distribution of the direction is mainly parallel to {100} but tilt an angle ~14.9° (ref. 35), which can be seen clearly from {010} direction. The folded IPF in Fig. 4c also shows an orientation tilt ~14.9°. These EBSD results confirm that the ARPRS technology is a fast, accurate, and non-destructive directional technology to identify the in-plane orientation of the SnS crystal.

Furthermore, temperature-dependent Raman spectroscopy is a useful method to study the thermal expansion and thermal conductivity properties of the anisotropic SnS bulk.[36] Firstly, the laser-power dependent Raman spectroscopy results in Fig. S4† were carried out to show that lower incident laser power should be used to avoid any additional thermal effects. Then we
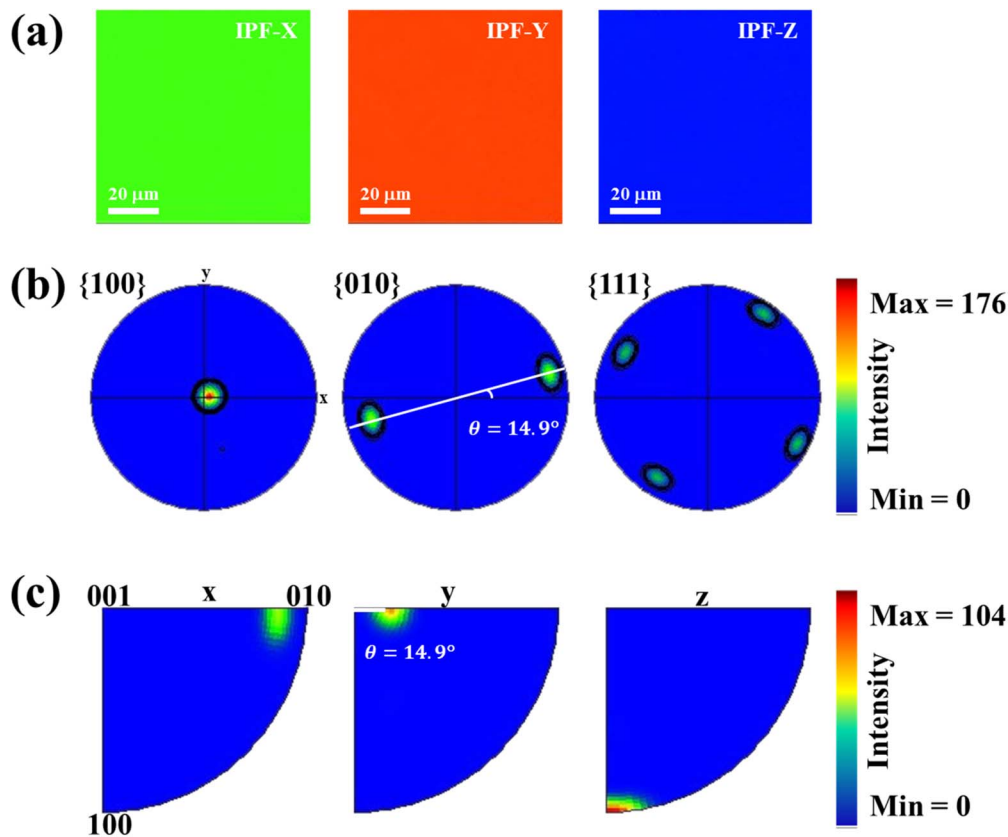
Fig. 4   .EBSD pole figure analysis from the in-plane center region of the SnS single crystal. (a) IPF maps from each axis in the center region of sample. (b) Pole figures and (c) folded pole figures.

systematically investigated the temperature-dependent Raman behavior of SnS by Nd:YAG excitation laser (532 nm), as shown in Fig. 5 at the temperature range from 77 to 425 K in a vacuum chamber.

Fig. 5a show that all B_{3g} and A_g Raman modes red-shift and the full width at half maximum (FWHM) of those modes increases with the rising temperature. The measured
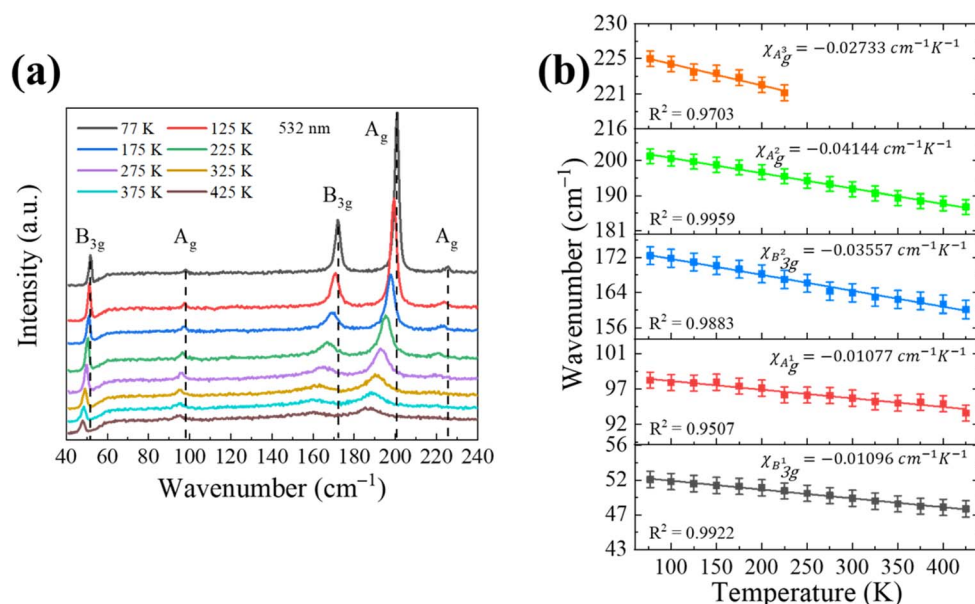

Fig. 5   .(a) In situ Raman spectra of SnS single crystal excited by 532 nm from 77 to 425 K on the cleavage plane. (b) Temperature dependence of the Raman peak positions and the corresponding fit (solid lines).

Table 2 Temperature-dependent coefficients of SnS and other materials

Materials	λ_{laser} (nm)	Raman modes	χ (cm^{-1} K^{-1})	Ref.
Single-layer graphene	488	G band	−0.016	38
Bi-layer graphene		G band	−0.015	
Monolayer MoS$_2$	514.5	E$^1_{2g}$	−0.011	39
		A$_{1g}$	−0.013	
Few-layer MoS$_2$	532	E$^1_{2g}$	−0.0132	40
Monolayer WS$_2$	532	A^1_g	−0.0149	41
		E$^1_{2g}$	−0.0125	
Bilayer WS$_2$		A^1_g	−0.0121	
		E$^1_{2g}$	−0.0133	
Single-layer MoSe$_2$	514.5	A^1_g	−0.0054	42
		A$^2_{2u}$	−0.0086	
Three-layer MoSe$_2$		A^1_g	−0.0045	
		A$^2_{2u}$	−0.0085	
SnSe single crystal	532	B$_{3g}$	−0.041	36
		A^2_g	−0.043	
		A^3_g	−0.014	
SnS single crystal	532	B$_{3g}$	−0.011	This work
		A^1_g	−0.011	
		B$_{3g}$	−0.036	
		A^2_g	−0.041	
		A^3_g	−0.027	

temperature dependence of the Raman mode frequency shift in the SnS can be characterized by a linear equation:

$$\omega = \omega_0 + \chi T$$

where ω_0 is the mode frequency at 0 K and χ is the first-order temperature coefficient. Fig. 5b showed that the measured χ values for modes B$^1_{3g}$, A^1_g, B$^2_{3g}$ A^2_g and A^3_g in the bulk are −0.01096, −0.01077, −0.03557, −0.04144 and −0.02733 cm^{-1} K^{-1} for 532 nm laser excitation, respectively. Here we ignore the higher order temperature coefficient in our results due to its weak effect at low temperature. Interestingly, it can be found that out-of-plane vibration mode A^2_g of SnS has much larger $|\chi|$ than that of in-plane vibration modes (B$^1_{3g}$, B$^2_{3g}$ and A^3_g). The weak interlayer van der Waals forces along the a-axis give rise to soft optical modes, which in turn can couple with the heat carrying acoustic phonons and then enhance the phonon scattering, thereby reducing the lattice thermal conductivity.[22,37] Furthermore, soft Raman modes are intimately related to the vibration directions. We also compared the first-order temperature coefficients of SnS with that of other famous layered materials such as graphene[38] and TMDs[39–42] shown in Table 2. As a result, the first-order temperature coefficient of Raman mode can be regarded as an indicator of thermal expansion because the shifting of Raman peak is in a reasonably good agreement with the variation of lattice parameters with the change of temperature.

Conclusions

In conclusion, we observed the strong anisotropy of SnS single crystal through ARPRS technology. The results were fitted and matched well with the classical Raman scattering theory, which

showed different periodic properties depending on the excitation wavelengths and polarization configurations. The ARPRS along with EBSD technologies in the present study provide very useful information to quickly determine the in-plane crystallographic orientations of SnS and further improve the accuracy. The temperature coefficients from Raman can be used to distinguish the in-plane and out-of-plane modes. All obtained results can be applied for further analysis of SnS and other van der Waals layered materials for real devices in the future.

Author contributions

X. G. conceived the idea and discussed with T. Y., J. L., C. Y., J. L. H. Z., B. Z., H. W., Z. Z. and X. Z.; X. G. performed characterizations, analysed all data. T. Y. and J. L. carried out polarized Raman measurements and analysed the data. H. W. performed materials synthesis, DFT calculation. J. L. and B. Z. performed the HRTEM measurement and analysed the data. H. Z. performed the XRD measurement and analysed the data. X. G. wrote the preliminary draft and revised the manuscript. X. G., H. W., Z. Z., and X. Z. discussed the results and revised the manuscript. All authors contributed to interpreting the findings, reviewing, and commenting on the manuscript.

Conflicts of interest

There are no conflicts to declare.

Acknowledgements

Notes and references

1 W. He, D. Wang, H. Wu, Y. Xiao, Y. Zhang, D. He, Y. Feng, Y. J. Hao, J. F. Dong, R. Chetty, L. Hao, D. Chen, J. Qin, Q. Yang, X. Li, J. M. Song, Y. Zhu, W. Xu, C. Niu, X. Li, G. Wang, C. Liu, M. Ohta, S. J. Pennycook, J. He, J. F. Li and L. D. Zhao, *Science*, 2019, **365**, 1418–1424.

2 K. Liang, L. Ju, S. Koul, A. Kushima and Y. Yang, *Adv. Energy Mater.*, 2019, **9**, 1802543.

3 H. Tian, C. Fan, G. Liu, S. Yuan, Y. Zhang, M. Wang and E. Li, *Appl. Surf. Sci.*, 2019, **487**, 1043–1048.

4 L. A. Burton, D. Colombara, R. D. Abellon, F. C. Grozema, L. M. Peter, T. J. Savenije, G. Dennler and A. Walsh, *Chem. Mater.*, 2013, **25**, 4908–4916.

5 J. R. Brent, D. J. Lewis, T. Lorenz, E. A. Lewis, N. Savjani, S. J. Haigh, G. Seifert, B. Derby and P. O'Brien, *J. Am. Chem. Soc.*, 2015, **137**, 12689–12696.

6 H. Wu, X. Lu, G. Y. Wang, K. L. Peng, H. Chi, B. Zhang, Y. J. Chen, C. J. Li, Y. C. Yan, L. J. Guo, C. Uher, X. Y. Zhou and X. D. Han, *Adv. Energy Mater.*, 2018, **8**, 1800087.

7 X.-L. Liu, X. Zhang, M.-L. Lin and P.-H. Tan, *Chin. Phys. B*, 2017, **26**, 067802.

8 J. Wu, N. Mao, L. Xie, H. Xu and J. Zhang, *Angew. Chem., Int. Ed.*, 2015, **54**, 2366–2369.

9 X. Xu, Q. Song, H. Wang, P. Li, K. Zhang, Y. Wang, K. Yuan, Z. Yang, Y. Ye and L. Dai, *ACS Appl. Mater. Interfaces*, 2017, **9**, 12601–12607.

10 L. Li, P. Gong, W. Wang, B. Deng, L. Pi, J. Yu, X. Zhou, X. Shi, H. Li and T. Zhai, *ACS Nano*, 2017, **11**, 10264–10272.

11 J. Kim, J. U. Lee, J. Lee, H. J. Park, Z. Lee, C. Lee and H. Cheong, *Nanoscale*, 2015, **7**, 18708–18715.

12 J. Lee, T. Y. Ko, J. H. Kim, H. Bark, B. Kang, S. G. Jung, T. Park, Z. Lee, S. Ryu and C. Lee, *ACS Nano*, 2017, **11**, 10935–10944.

13 N. Fleck, T. D. C. Hobson, C. N. Savory, J. Buckeridge, T. D. Veal, M. R. Correia, D. O. Scanlon, K. Durose and F. Jäckel, *J. Mater. Chem. A*, 2020, **8**, 8337–8344.

14 Q. Song, X. Pan, H. Wang, K. Zhang, Q. Tan, P. Li, Y. Wan, Y. Wang, X. Xu, M. Lin, X. Wan, F. Song and L. Dai, *Sci. Rep.*, 2016, **6**, 29254.

15 G. M. Sheldrick, *Acta Crystallogr., Sect. C: Struct. Chem.*, 2015, **71**, 3–8.

16 O. V. Dolomanov, L. J. Bourhis, R. J. Gildea, J. A. K. Howard and H. Puschmann, *J. Appl. Crystallogr.*, 2009, **42**, 339–341.

17 G. Kresse and J. Furthmuller, *Phys. Rev. B: Condens. Matter Mater. Phys.*, 1996, **54**, 11169–11186.

18 G. Kresse and D. Joubert, *Phys. Rev. B: Condens. Matter Mater. Phys.*, 1999, **59**, 1758–1775.

19 P. E. Blochl, *Phys. Rev. B: Condens. Matter Mater. Phys.*, 1994, **50**, 17953–17979.

20 J. P. Perdew, K. Burke and M. Ernzerhof, *Phys. Rev. Lett.*, 1996, **77**, 3865–3868.

21 A. Togo and I. Tanaka, *Scr. Mater.*, 2015, **108**, 1–5.

22 L. Xu, W. Wang, Q. Xie, C. Hu, L. Chen, J. Zheng, H. Yin, G. Cheng and X. Ai, *J. Raman Spectrosc.*, 2021, **53**, 104–112.

23 H. R. Chandrasekhar, R. G. Humphreys, U. Zwick and M. Cardona, *Phys. Rev. B: Solid State*, 1977, **15**, 2177–2183.

24 X. Zhang, Q. H. Tan, J. B. Wu, W. Shi and P. H. Tan, *Nanoscale*, 2016, **8**, 6435–6450.

25 R. Guo, X. Wang, Y. Kuang and B. Huang, *Phys. Rev. B: Condens. Matter Mater. Phys.*, 2015, **92**, 115202.

26 D. Yoon, Y. W. Son and H. Cheong, *Phys. Rev. Lett.*, 2011, **106**, 155502.

27 H. Liu, A. T. Neal, Z. Zhu, Z. Luo, X. Xu, D. Tomanek and P. D. Ye, *ACS Nano*, 2014, **8**, 4033–4041.

28 F. Xia, H. Wang and Y. Jia, *Nat. Commun.*, 2014, **5**, 4458.

29 R. Loudon, *Adv. Phys.*, 2001, **50**, 813–864.

30 M. M. Nowell, M. A. Scarpulla, N. R. Paudel, K. A. Wieland, A. D. Compaan and X. Liu, *Microsc. Microanal.*, 2015, **21**, 927–935.

31 J. Kamimura, M. Ramsteiner, U. Jahn, C.-Y. James Lu, A. Kikuchi, K. Kishino and H. Riechert, *J. Phys. D: Appl. Phys.*, 2016, **49**, 155106.

32 A. Winkelmann, G. Cios, T. Tokarski, G. Nolze, R. Hielscher and T. Kozieł, *Acta Mater.*, 2020, **188**, 376–385.

33 N. Schafer, A. J. Wilkinson, T. Schmid, A. Winkelmann, G. A. Chahine, T. U. Schulli, T. Rissom, J. Marquardt, S. Schorr and D. Abou-Ras, *Ultramicroscopy*, 2016, **169**, 89–97.

34 T. Schmid, N. Schafer, S. Levcenko, T. Rissom and D. Abou-Ras, *Sci. Rep.*, 2015, **5**, 18410.

35 L. D. Zhao, S. H. Lo, Y. Zhang, H. Sun, G. Tan, C. Uher, C. Wolverton, V. P. Dravid and M. G. Kanatzidis, *Nature*, 2014, **508**, 373–377.

36 X. Gong, H. Wu, D. Yang, B. Zhang, K. Peng, H. Zou, L. Guo, X. Lu, Y. Chai, G. Wang and X. Zhou, *Vib. Spectrosc.*, 2020, **107**, 103034.

37 M. Dutta, D. Sarkar and K. Biswas, *Chem. Commun.*, 2021, **57**, 4751–4767.

38 I. Calizo, A. A. Balandin, W. Bao, F. Miao and C. N. Lau, *Nano Lett.*, 2007, **7**, 2645–2649.

39 R. Yan, J. R. Simpson, S. Bertolazzi, J. Brivio, M. Watson, X. Wu, A. Kis, T. Luo, A. R. Hight Walker and H. G. Xing, *ACS Nano*, 2014, **8**, 986–993.

40 S. Sahoo, A. P. S. Gaur, M. Ahmadi, M. J. F. Guinel and R. S. Katiyar, *J. Phys. Chem. C*, 2013, **117**, 9042–9047.

41 N. Peimyoo, J. Shang, W. Yang, Y. Wang, C. Cong and T. Yu, *Nano Res.*, 2014, **8**, 1210–1221.

42 D. J. Late, S. N. Shirodkar, U. V. Waghmare, V. P. Dravid and C. N. Rao, *ChemPhysChem*, 2014, **15**, 1592–1598.